IEEE Photonics Journal
An IEEE Photonics Society Publication

Modeling and Analysis of an 80-Gbit/s SiGe HBT Electrooptic Modulator

Volume 3, Number 1, February 2011

Tuhin Guha Neogi, Student Member, IEEE
Shengling Deng, Student Member, IEEE
Joseph Novak, Student Member, IEEE
Jong-Ru Guo
Ryan Clarke, Student Member, IEEE
Mitchell R. LeRoy, Student Member, IEEE
John F. McDonald, Life Senior Member, IEEE
Zhaoran Rena Huang, Member, IEEE

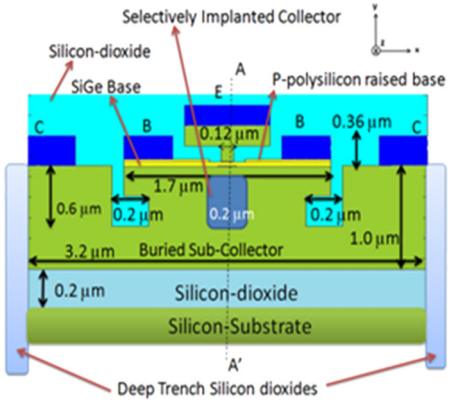

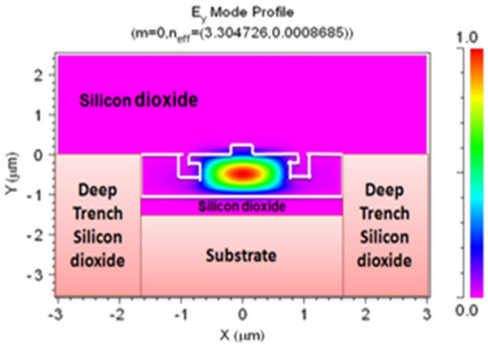

DOI: 10.1109/JPHOT.2010.2100038
1943-0655/$26.00 ©2010 IEEE

Modeling and Analysis of an 80-Gbit/s SiGe HBT Electrooptic Modulator

Tuhin Guha Neogi,[1] *Student Member, IEEE, Shengling Deng,[1] Student Member, IEEE, Joseph Novak,[1] Student Member, IEEE*, Jong-Ru Guo,[2] Ryan Clarke,[1] *Student Member, IEEE*, Mitchell R. LeRoy,[1] *Student Member, IEEE*, John F. McDonald,[1] *Life Senior Member, IEEE*, and Zhaoran Rena Huang,[1] *Member, IEEE*

[1]Electrical, Computer, and Systems Engineering Department, Rensselaer Polytechnic Institute, Troy, NY 12180 USA
[2]IBM Microelectronics, East Fishkill, NY 12533 USA

DOI: 10.1109/JPHOT.2010.2100038
1943-0655/$26.00 ©2010 IEEE

Manuscript received November 8, 2010; revised December 6, 2010; accepted December 9, 2010. Date of publication December 16, 2010; date of current version January 24, 2011. Corresponding author: T. Guha Neogi (e-mail: guhant@rpi.edu).

Abstract: We present a rigorous electrical and optical analysis of a strained and graded base SiGe Heterojunction Bipolar Transistor (HBT) electrooptic (EO) modulator. In this paper, we propose a 2-D model for a graded base SiGe HBT structure that is capable of operating at a data bit rate of 80 Gbit/s or higher. In this structure, apart from a polysilicon/monosilicon emitter (Width $= 0.12$ μm) and a strained SiGe graded base (Depth $= 40$ nm), a selectively implanted collector (SIC) (Depth $= 0.6$ μm) is introduced. Furthermore, the terminal characteristics of this new device modeled using MEDICI are closely compared with the SiGe HBT in the IBM production line, suggesting the possibility of fast deployment of the EO modulator using established commercial processing. At a subcollector depth of 0.4 μm and at a base-emitter swing of 0 to 1.1 V, this model predicts a rise time of 5.1 ps and a fall time of 3.6 ps. Optical simulations predict a π phase shift length (L_π) of 240.8 μm with an extinction ratio of 7.5 dB at a wavelength of 1.55 μm. Additionally, the tradeoff between the switching speed, L_π and propagation loss with a thinner subcollector is analyzed and reported.

Index Terms: Semiconductor device modeling, integrated optics, optical modulation, plasma dispersion effect, SiGe, Heterojunction Bipolar Transistors (HBTs).

1. Introduction

Fast modulation of optical signals with low-cost devices is of great interest to many fields, ranging from on-chip or intra-chip interconnections to Si photonics for telecommunication. Among the different technologies explored in developing modulators, silicon photonics is one of the most promising as it allows mass production at an attractive cost and monolithic integration with advanced electronics on a single die [1]. Electrooptical effects in strained silicon [2] or quantum-confined stark effect in SiGe/Ge quantum wells [3] have been demonstrated recently, but current high-speed modulators integrated in silicon are based on the plasma dispersion effect [4] and have been amply verified by experimental measurements. In 1997, a three-terminal Bipolar Mode FET (BMFET) integrated in a low-loss single-mode Silicon-on-Insulator (SOI) waveguide was proposed, having a switching time of less than 3.5 ns and a π-phase shift interaction length (L_π) of 1 mm [5]. In 2007, IBM reported a P-I-N silicon modulator with bit rates of 10 Gbit/s and an L_π of 100 to 200 μm [5]. In the same year, Intel demonstrated a PN junction based high speed modulator of 40 Gbit/s with

an L_π of 1 mm in a Mach–Zehnder Interferometer (MZI) configuration using a carrier depletion structure combined with travelling wave electrodes [7]. In 2005, a depletion mode PN junction based SOI modulator was reported with rise and fall times of 7 ps with an effective bandwidth of 60 GHz [8]. In the same year, a shorter electrooptic (EO) modulator length was demonstrated by incorporating resonant light-confining structures [9]. III–V based traveling wave electro-absorption modulators (TWEAM) using the high quantum-confined stark effect has been reported to operate at 80–100 Gbit/s [25]. Modeling of a silicon modulator with an operation bandwidth of 74 GHz using a metal–oxide–semiconductor (MOS) capacitor structure in a ring resonator configuration was reported in 2009 [27]. In 1990, Soref proposed the use of SiGe-on-Si technology for high-speed optical modulation based on a free carrier plasma effect [10]. The SiGe modulators reported in the literature exhibited longer device lengths and *RC* limited bandwidths [11], [12]. Several of these papers provide experimental verification that the free carrier effect can be utilized. The question that remains now is how fast this effect can operate and with what physical length, propagation loss, and energy per bit.

Our previous work on a SiGe Heterojunction Bipolar Transistor (HBT) EO modulator reported an operation bandwidth limited to 2.4 GHz [24] and 10.5 GHz with a short L_π of 73.6 μm [19]. In this new structure explored by MEDICI, we designed the doping concentration of all three regions, namely emitter, base, and collector, and added mono-crystalline silicon to enhance carrier mobility which appears to be critical in improving the speed of the device. The reduction in the lateral width of the transistor resulted in lower intrinsic base resistance, extrinsic base resistance, and emitter-base and base-collector intrinsic capacitances. The key contribution of this study is the improvement in the rise and fall times of the EO modulator during large signal switching. This is achieved by the introduction of mono-crystal silicon layer on the thin SiGe epitaxial base and the compressively strained SiGe base on the selectively implanted collector (SIC). The rise time is improved by enhancing the mobility of both the electrons and holes in the base. The monosilicon cap layer and the graded Ge base, which introduces a built in electric field, accelerate the vertical transport of electrons. The compressive strain in the SiGe base enhances the lateral and vertical hole mobility. The fall time is improved due to the smaller recombination lifetime in the reduced bandgap SiGe base and lesser charge storage in the polysilicon emitter. However, the thickness of the base is limited by the punch-through effects due emitter-base and base-collector depletion capacitances. This limited thickness also limits the strain induced mobility enhancement. A thinner base reduces the base transit time of the electrons but, at the same time, reduces the overlap of the optical field with the carriers and, hence, the modulation efficiency. Additionally, at extremely thin bases (below 20 nm), the numerical simulation techniques used should accurately model the transport of highly energetic electrons and holes.

In this paper, we also analyze the terminal characteristics of the HBT, namely small signal cutoff frequency, current gain, and transient response. A close match is obtained in comparison with npn HBTs using IBM's 8HP technology [14], studied by CADENCE simulator. This suggests that the modulator is manufacturable using the IBM 8HP fabrication process through the brokerage service provider MOSIS [22].Two independent device and circuit simulation tools have been employed at each step of the simulation to cross check the results wherever possible. These simulations strongly support the primary conclusion of this study that the proposed SiGe EO modulator can operate at 80 Gbit/s or perhaps beyond. To confirm that the rise and fall time of the EO modulator is only a few picoseconds, we study the time evolution of the free carrier plasma including both electrons and holes in the device. In addition, we verify that the SiGe HBT waveguide is single mode at both zero bias and high bias $(V_{be} = 1.1\ \text{V})$. The extinction ratio of the MZI, the dynamic power consumption, and the attenuation of the wave propagation are also computed in this paper. Finally, the tradeoff between the waveguide propagation loss and the device speed as a result of thinning of the subcollector region is analyzed. The viability of a SiGe-based modulator is supplemented by the feasibility of an 80–100 GHz photodetector using a p-Ge/i-Si/n-Si heterojunction PIN diode [27]. To the best of our knowledge, it is the fastest Si EO modulator ever proposed based on the free-carrier plasma effect. Moreover, by using an MZI configuration, the proposed EO modulator has provided much better temperature stability compared with ring or disk resonator based Si EO modulators [9], [30].

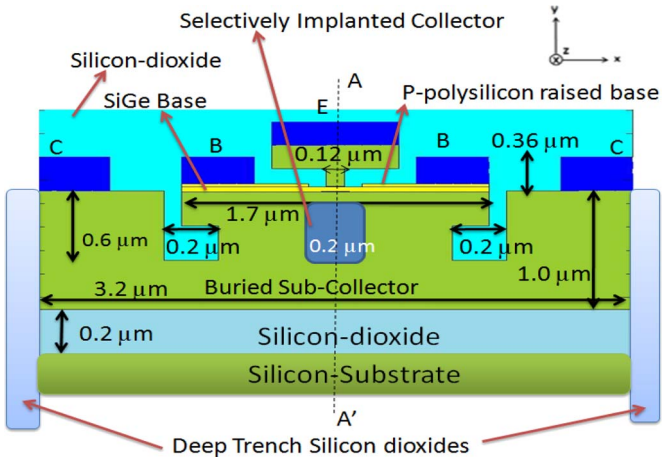

Fig. 1. Schematic cross-section of the proposed HBT EO modulator model.

2. Device Structure

The proposed 2-D HBT device structure is shown in Fig. 1. The typical parameters that represent the HBT technology are the base thickness and the emitter width (W_E). In this model, an n-doped Polysilicon Emitter with uniform doping concentration of 1×10^{21} cm^{-3}, width of 0.12 μm, and depth of 0.36 μm is chosen. There are two symmetric base contacts and two symmetric collector contacts on each side of the emitter. This configuration is chosen because of superior driving ability, lower thermal resistance, and lower sensitivity to self-heating [17]. The base consists of p-doped strained SiGe alloy with a thickness of 40 nm and width of 1.7 μm. The germanium mole fraction is linearly graded from 19% at Emitter-Base junction to 25% at Base-Collector junction [14]. The thin epitaxial base has a peak doping of 5.5×10^{19} cm^{-3}. A highly doped p-Polysilicon $(3 \times 10^{20}$ cm$^{-3})$ raised extrinsic base with a thickness of 80 nm and width of 0.7 μm is defined on each side of the narrow emitter. A narrow distance between the edge of emitter and the edge of raised extrinsic base is chosen to reduce the extrinsic base resistance. An SIC region with a thickness of 0.6 μm and width of 0.2 μm is incorporated. The peak doping level of 8×10^{18} cm^{-3} is chosen in the SIC with a downward gradient toward the base. The remaining part of the low doped (N^-) collector region assumes the background doping of 2×10^{16} cm^{-3} on each side of SIC. The buried subcollector of width 3.32 μm, depth of 0.4 μm and high doping concentration of 1.3×10^{19} cm^{-3} is defined to reduce the resistance of the subcollector region which connects the intrinsic BC junction to the collector contact. The reach-through layer connecting the subcollector layer and the collector contacts assumes a high doping of 2×10^{19} cm^{-3}. The doping profile along the center of the device cross-section (AA') is plotted in Fig. 2. A buried oxide layer with a thickness of 0.2 μm and width of 3.32 μm is assumed just below the subcollector. Fig. 1 assumes a silicon substrate below the buried oxide with a doping concentration of 2×10^{16} cm^{-3}. As shown in Fig. 1, there are two shallow trenches of 0.6 μm thickness below the base contacts. The two deep trenches are defined on each side of the collector contacts. These trenches are filled with silicon dioxide, which behaves as an electrical insulator and additionally confines the light due to its low refractive index compared with silicon.

3. Device Modeling

The electrical characteristics of the HBT EO modulator are explored by a 2-D simulation tool MEDICI. The key parameters examined include the free-carrier concentration and distribution. These parameters give rise to optical field confinement, injection current, DC characteristics, and electrical power at transient conditions. An optical model is created to design and analyze the mode confinement, π phase shift interaction length (L_π), transmission characteristics, modulation depth, and optical losses of the structure.

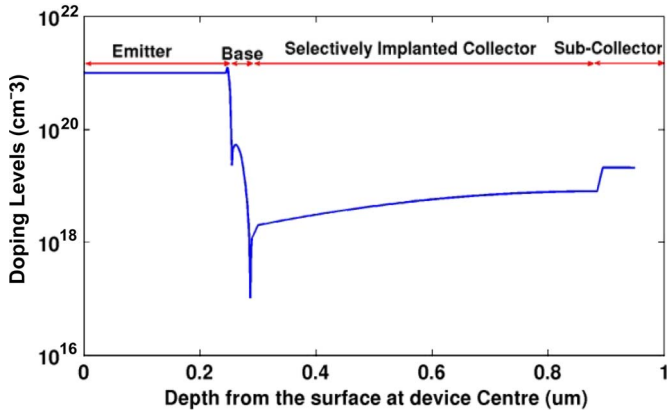

Fig. 2. Doping profile verse vertical distance at device center (AA') from the surface.

3.1. Electrical Model

The 2-D simulation package MEDICI from SYNOPSYS [14] is employed to analyze the electrical calculations of the proposed HBT device. Suitability of this device modeling software to analyze electrical performance in SOI waveguides has been demonstrated by other authors [5], [27]. This program simulates internal physics and device characteristics of semiconductor devices by solving Poisson's equation and the charge continuity equations for electrons and holes numerically. The software allows a complete statistical approach (Fermi-Dirac statistics) when, for example, heavily doped regions are considered. Carrier recombination models include Shockley–Read–Hall (SRH) recombination, Auger recombination, and surface recombination. A concentration dependent model has been used to determine the carrier mobility. In our simulations, the Philips unified model (PHUMOB) [14] and the velocity saturation models [14] are chosen for mobility calculation and to correctly represent the majority and minority carrier dynamics of a bipolar device. To account for the excess carrier recombination and the heavy doping effects throughout the device, the Slotboom bandgap narrowing (BGN) model [14], [16], the concentration dependent SRH model, and the Auger recombination model are included in these simulations [14]. The bandgap narrowing parameters for silicon, Polysilicon, and SiGe regions are carefully chosen for curve fitting. Ohmic contacts without additional contact resistance or capacitance have been assumed.

The accuracy of device simulation of SiGe HBTs is often determined by how accurately carrier transport is described. Three carrier transport models are now generally used: the drift-diffusion (DD) model, the hydrodynamic (HD) model, and the Monte Carlo (MC) model. Drift-diffusion model of charge transport neglects nonlocal transport effects such as velocity overshoot, diffusion associated with carrier temperature gradients, and the dependence of impact ionization rates on carrier energy distributions. The more detailed HD model approach includes the energy gradient in the current equation and considers mobility as a function of the average carrier energy. Local carrier heating in high and rapidly varying electric fields is modeled using a self-consistent solution of the drift-diffusion and carrier energy balance equations. These carrier energy balance equations are included by using the ET.MODEL statement in our proposed device [14]. The basic MC algorithm is based on the individual representation of a significant portion of the charge carrier population as computer particles. Hence, one advantage of this technique is its ability to depict a complete picture of carrier dynamics based on their microscopic material parameters, such as effective masses. MC simulation is considered to be the most accurate approach within the framework of semi-classical device physics but is not widely used due to its unattractive computing time. Hence, it was essential to adopt HD model in this study for accurate investigation at 80 Gbit/s.

Given the known Ge content and strain-induced changes to the energy, degeneracy, and local curvature of both the conduction and valence bands in Si, it is to be expected that both the carrier effective masses will be significantly altered in strained SiGe compared with their original Si values.

Because carrier transport parameters depend intimately on the band structure and the resultant carrier effective masses, all of the carrier transport parameters can be expected to change with the addition of Ge to Si. These occurrences are captured in the strained SiGe model statement SIGE (EG. MODEL = 2) [14]. These changes to the device transport parameters in SiGe are important because 1) the collector current in a SiGe HBT is proportional to the minority electron mobility in the base (τ_{nb}); 2) the base current is proportional to the minority hole mobility in the emitter; 3) the base transit time is reciprocally proportional to τ_{nb}; and 4) the base resistance, which is important in dynamic switching, is proportional to the hole mobility in the base. These facts are included in Philips unified model (PHUMOB) and the velocity saturation models [14].

In order to compare the terminal currents, forward current gain, Gummel characteristics, and output characteristics of our proposed device model to the IBM certified 8HP model [14], identical test circuits are constructed and simulated for both. For this particular work, simulations of the IBM 8HP models are performed in Virtuoso Analog Design Environment with SPECTRE: a simulator integrated with the circuit level schematic tool CADENCE. The simulations on our proposed model are performed using MEDICI: a device simulator from SYNOPSYS. The primary reason for adopting our proposed device model is to exhibit the spatial distribution of the carriers and their switching speed, which is not deducible from simulations of IBM 8HP models. Additionally, it provides us the ability to verify our model with the IBM 8HP model in production. The IBM published manual releases that the NPN SiGe HBT transistor of IBM 8HP has an emitter width 0.12 μm. In this paper, an emitter length of 2 μm is chosen for the SPECTRE simulations. The length is not applicable for MEDICI as it is a 2-D simulator. The temperature for the simulations is chosen as 85 °C.

3.2. Optical Model

We use the Beam Propagation method (BPM) [18] for the optical analysis of the wave propagation in the HBT waveguide. From the values of the electron and hole concentrations at any point of the SiGe HBT, the induced real refractive index and optical absorption coefficient variations are computed according to [4]

$$\Delta n = \Delta n_e + \Delta n_h = -\left[8.8 \times 10^{-22}\Delta N_e + 8.5 \times 10^{-18}(\Delta N_h)^{0.8}\right] \quad (1)$$

$$\Delta \alpha = \Delta \alpha_e + \Delta \alpha_h = [8.5 \times 10^{-18}\Delta N_e + 6.0 \times 10^{-18}\Delta N_h] \quad (2)$$

where Δn and $\Delta \alpha$ are the real part of refractive index and the absorption coefficient, respectively. In (1) and (2), ΔN represent the carrier density changes, with "e" and "h" denoting electron and hole, respectively. The refractive index files generated using the carrier distribution across the device are imported to the HBT waveguide constructed in the BPM software [18]. The background index in locations other than the device is assumed to be of silicon dioxide with refractive index 1.45. The use of crystalline Si (c-Si) instead of polysilicon or amorphous Si as the waveguide core reduces scattering and absorption losses [30]. Since the core of our waveguide lies in the base and the SIC region, scattering losses due to surface roughness are neglected. However, the scattering losses due to the change in free carrier plasma are incorporated. The fundamental mode of the waveguide is launched, and the L_π, propagation loss and extinction ratio are calculated. L_π is computed as $\lambda/2\Delta n_{eff}$, where λ is 1.55 μm, and Δn_{eff} is effective index variation of the optical channel.

4. Results and Discussion

4.1. Electrical Analysis

To characterize our model, it is imperative to consider the DC and small-signal characteristics. The cutoff frequency (f_t) versus collector current (I_c) curve illustrates the unity gain cutoff frequency of the device, which gives insight into the speed of operation. To characterize the behavior of the E-B and B-C junction capacitances, it is necessary to inspect the forward Gummel characteristics, the forward current gain, and the output characteristics of the device. The close match of our model to 8HP data confirms the feasibility of this model to be fabricated and tested experimentally

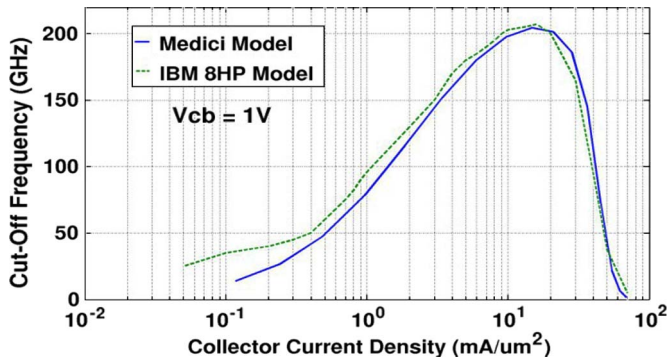

Fig. 3. Small-signal cutoff frequency of MEDICI model and IBM 8HP.

through MOSIS. To determine the switching speed of the EO modulator, the large signal dynamic performance and the time evolution of the electron/hole carrier density of the device are computed.

4.1.1. Small Signal Cutoff Frequency

Vertical scaling of HBTs is often given higher priority than lateral scaling. In bipolar design, base thickness and its representative scaling parameter are of the highest importance. A thinner base leads to reduced minority carrier transit time and enhanced built-in electric field. A base thickness of 40 nm is carefully chosen in our model to push the peak cutoff frequency (f_t) to 205 GHz, as illustrated in Fig. 3. The collector current density (I_C) corresponding to the peak cutoff frequency is 14.6 mA/μm^2 at V_{cb} of 1 V. For a typical 8HP HBT device, the peak cutoff frequency is in excess of 200 GHz at $I_C \approx$ 8–16.5 mA/μm^2 [14]. The roll-off in the curve beyond f_t was obtained by tuning the SIC retrograde doping level and shape. A higher peak doping in the SIC pushes the onset of high injection condition to higher collector current densities. To control the rate of roll-off in the f_t versus I_c curve, the slope of the SIC retrograde profile is adjusted to 1.3×10^{17} cm$^{-3}/\mu$m. The lower slope of the retrograde profile resulted in a steeper roll-off in the f_t versus I_c curve. With the existing device parameters assigned to our model, it can be concluded that the AC behavior of our model is very close to the IBM 8HP CADENCE small-signal model, hence proving the validity of our structure and small-signal model parameters.

4.1.2. Comparison of Forward Gummel, Current Gain, and Output Characteristics

To analyze the operation of E-B junction, the forward Gummel characteristics is extracted from CADENCE and MEDICI by applying a V_{be} sweep from 0 to 1 V with $V_{cb} = 0$ V. The extracted plots when superimposed further confirm good accuracy for our model. This is illustrated in Fig. 4. The slotboom bandgap narrowing model is used to illustrate the high doping effects bandgap narrowing in the SiGe HBT. According to the slotboom model, the bandgap of a semiconductor material is given by (3) [14], [16]:

$$\Delta E_g = \frac{V0 \times q}{2kT}\left[\ln\frac{N_{total}}{N0} + \sqrt{\left(\ln\frac{N_{total}}{N0}\right)^2 + k}\right] \tag{3}$$

where ΔE_g is the bandgap change due to heavy doping effects, N_{total} is the intrinsic doping level used in the device (Fig. 2), and k is Boltzmann's constant. High doping bandgap narrowing model parameters includes a voltage parameter $V0$, a constant parameter k, and a concentration parameter $N0$. The parameter values are chosen to be $V0$ of 5.9×10^{-3}, $N0$ of 1.3×10^{17}, and k of 0.5 for Si and SiGe regions. To illustrate the recombination mechanism in the base, the electron (τ_{n0}) and hole (τ_{p0}) bulk lifetime parameters were chosen as 2×10^{-5} s and 2×10^{-5} s, respectively [14]. At V_{be} biases below 0.15 V, the collector and base currents start at equal values of

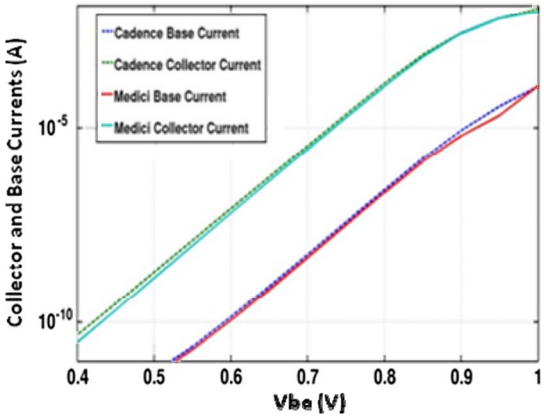

Fig. 4. Forward Gummel plot of MEDICI model and IBM 8HP model.

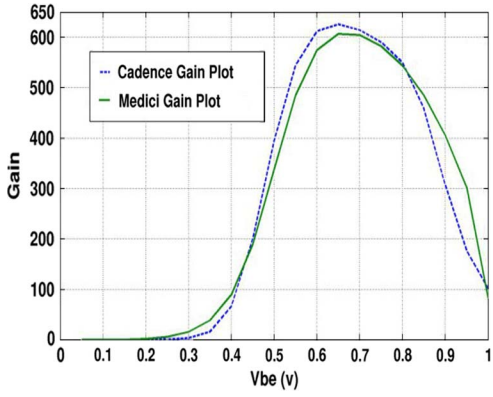

Fig. 5. Forward Current Gain of MEDICI and IBM 8HP model.

10^{-14} A. The dominant component of base current at biases lower than 0.4 V is due to recombination rather than diffusion of carriers. Hence, the lifetime parameters played a critical role at those bias levels.

As the forward bias is increased to 0.4 V, the collector current increases more rapidly than the base current. This is because of the heterojunction base, resulting in a forward current gain, as shown in Fig. 5. The output characteristics of the SiGe HBT are extracted by applying a fixed V_{be} of 0.9 V, 1 V, and 1.1 V while sweeping V_{ce} from 0 V to 0.8 V, as shown in Fig. 6.

4.1.3. Comparison of Transient Response of the Terminal Currents

After validation of the small signal and DC characteristics, it is necessary to validate the transient response of the device to verify the switching speed. The base doping profile in Fig. 2 was adopted. The terminal currents are illustrated in Fig. 7. To perform this experiment, a square pulse of 0 to 0.9 V with 1 ps ramp-up time is applied at the base of the transistor in Common-Emitter configuration with collector to emitter voltage (V_{ce}) of 0.5 V. This ensures that the device is switching from cutoff to saturation during the "ON" phase of 12.5 ps and saturation to cutoff during "OFF" phase of 12.5 ps. Based on our model, the transient peaks of the base, emitter, and collector currents at the ramp-up indicate the turn on of the emitter base junction and, hence, the criticality of emitter and base doping levels. The transient peaks during ramp-down of V_{be} illustrate the removal of the charge stored in the base. These current components are strongly dependant on the SRH recombination lifetime parameters. The steady-state currents are representative of the current gain of the device. A

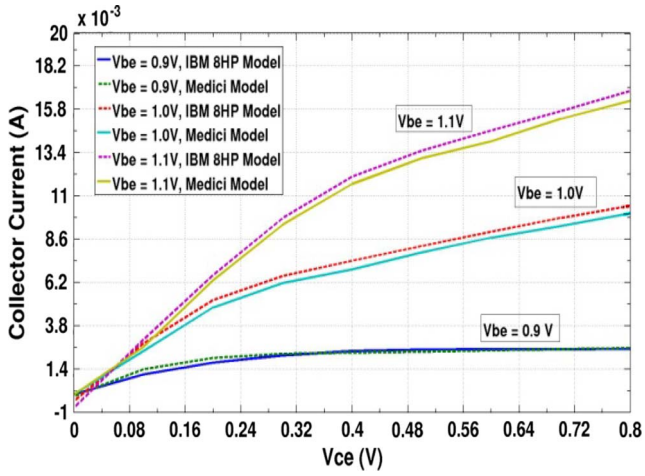

Fig. 6. Ouput IV characteristics of MEDICI model and IBM 8HP model.

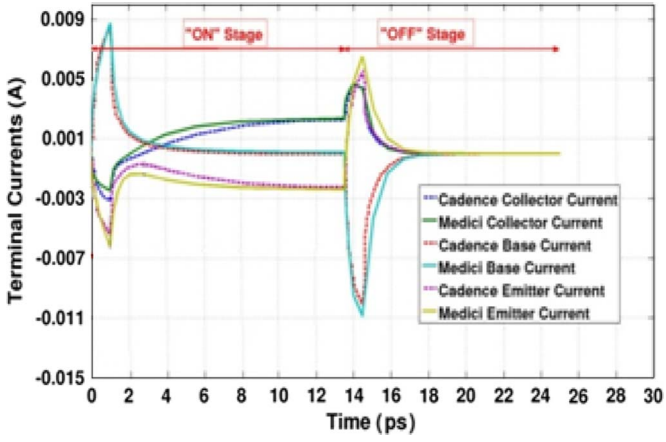

Fig. 7. Transient terminal currents MEDICI model compared IBM 8HP model to IBM 8HP model.

complete comparison of the MEDICI and CADENCE transient curves is in Fig. 7. In this figure, the collector current curve of our MEDICI model displays the rise and fall time as 4.7 and 3.4 ps, respectively, which is very close to the IBM 8HP CADENCE model.

The switching speed of the SiGe HBT is determined by the B-E and B-C junction capacitances; the emitter, base and collector resistances; and the diffusion capacitances. Because the transistor is operating as a large signal device, the depletion capacitances and the diffusion capacitances will vary as transistor moves from cutoff to saturation through the active region.

This model predicts a much faster switching speed compared with our previous model [19]. This can be attributed to higher doping used in the emitter, base, and collector, resulting in much lower intrinsic resistances. The presence of thin mono-crystal silicon (10 nm) and a thinner base (40 nm) also assist in reducing the transit time of the electrons when compared with the previously reported device in [19]. For the device without the mono-crystal silicon, a transit delay is observed at the emitter-base junction due to the low mobility of the grain boundary interface with the SiGe base. However, the mono-crystal silicon-cap interface with SiGe base is devoid of the grain boundaries and, hence, offers lower emitter resistance [29]. In addition, a lateral width of 3.32 μm between the two collector contacts is much smaller than the 6.8 μm reported in our previous work. This results in reduced base and collector resistances and smaller emitter-base and collector-base junction areas,

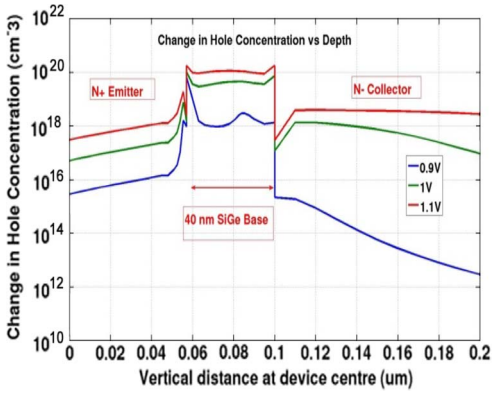

Fig. 8. Spatial distribution of the change in hole concentration for $V_{be} = 0.9$ V, 1.0 V, and 1.1 V.

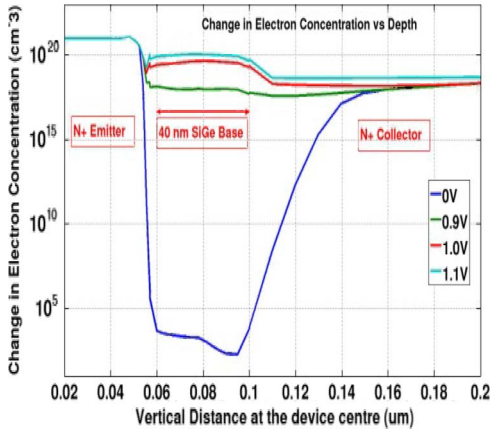

Fig. 9. Spatial distribution of the change in electron for $V_{be} = 0$ V, 0.9 V, 1.0 V, and 1.1 V.

thereby reducing the associated capacitances. Because of this, the RC time constant decreases which results in reduced switching time.

4.2. Transient Analysis of the Switching Speed of the Carriers

The steady-state hole and electron distribution of the MEDICI model under bias of V_{be} of 0.9 V, 1.0 V, and 1.1 V is shown in Figs. 8 and 9, respectively. At 1.1 V, the peak change in electron concentration in the base is 1×10^{20} cm^{-3} while the peak change in hole concentration is 1×10^{20} cm^{-3}. This change in concentration of the electrons and holes is used to compute the L_{π} of the device, as explained in Section 4.3.

The change in electron and hole concentrations illustrated in Figs. 8 and 9 denote the carrier density at the various bias levels. To satisfy the charge neutrality requirement in the collector, there is a significant increase in hole concentration in response to the high-level injection of electrons. The injection and removal of holes in the collector region also contribute to a change in refractive index. Because holes are considered slow carriers, it is important to study the time evolution of the charges in order to verify that the rise and fall times are on the order of picoseconds. The following Fig. 10(a) and (b) show the electron concentration rise and fall, respectively, with time at the center of device $(x = 0\ \mu\text{m})$ at $V_{be} = 1.1$ V. Similarly, Fig. 10(c) and (d) denote the hole concentration rise and fall, respectively, with time at the center of device. It can be observed from Fig. 10(a) and (c) that the electron and hole concentrations rise to about 1% of the maximum in 4 ps and 90% of the maximum in about 9.1 ps. This corresponds to 5.1 ps of rise time (t_r). Similarly, Fig. 10(b) and (d) illustrate the electron and hole concentration fall to 90% in 1.2 ps and to 1% in 4.8 ps. This

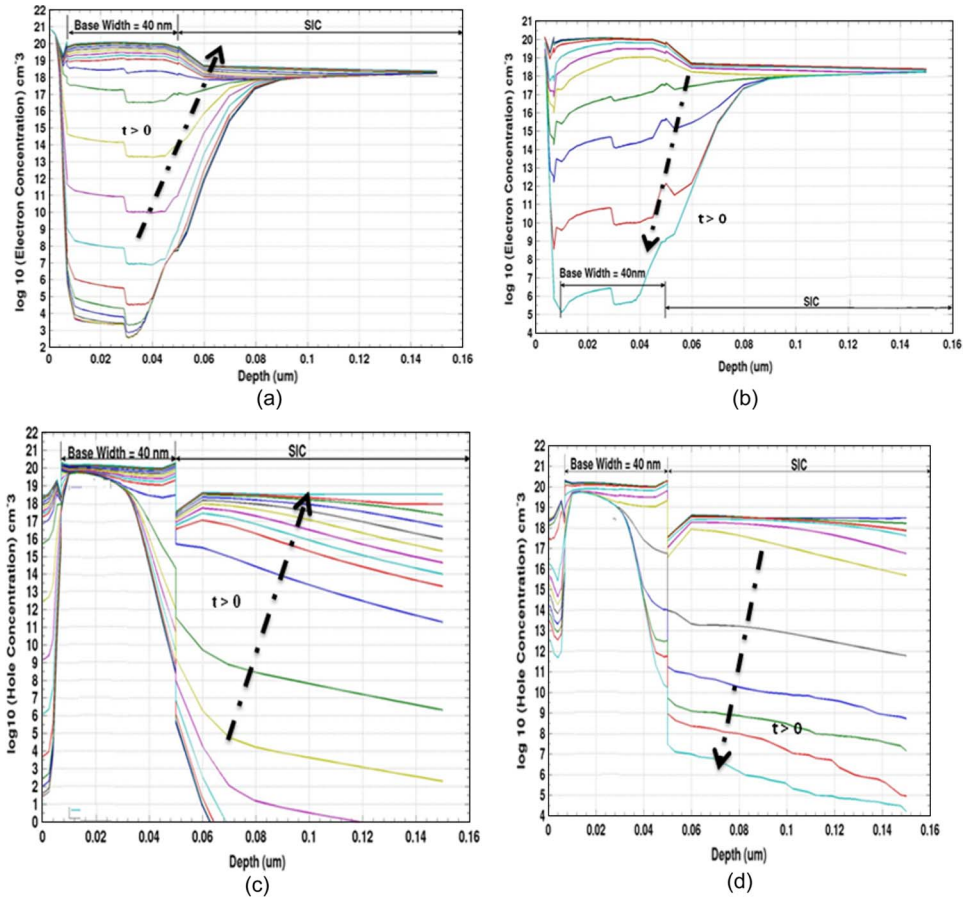

Fig. 10. Time evolution of free carriers for $V_{be} = 0$ to 1.1 V. (a) Electron Rise Time, step = 0.5 ps. (b) Electron Fall Time, step = 0.6 ps. (c) Hole Rise Time, step = 0.5 ps. (d) Hole Fall time, step = 0.6 ps.

corresponds to a fall time (t_f) of 3.6 ps. We chose the baseline carrier concentration to be 1% of the maximum charge density to get an optimal extinction ratio. The most important point to note is that the maximum concentration of free carriers denoted in Figs. 8 and 9 corresponds to the maximum concentration of carriers in the base and the SIC, as denoted in Fig. 10. The distribution of the charge build-up in the base and SIC determines the L_π of the modulator.

Considering the rise and fall times discussed above, the modulation speed in gigahertz is defined as the inverse of the sum of switch delays $1/(t_r + t_f)$. Hence, the modulation speed or the 3-dB bandwidth is 114 GHz. This corresponds to a data bit rate of 228 Gbit/s. However, there will be additional switching delay caused by the finite rise and fall time of the input driving signals. We estimate this adds an extra delay of $\sim$2 ps to $\sim$3 ps, which gives a total delay of $\sim$14 ps in circuit implementation of the proposed SiGe HBT EO modulator. Additional bandwidth budget is given to the consideration of full extinction ratio, which requires complete carrier injection and removal in the device. Thus, conservatively, we estimate the proposed HBT EO modulator to have an operation speed of 80 Gbit/s.

Parasitic resistances and capacitances introduced by the electrical contact pads required for longer length of the device will degrade the operational bandwidth. One way to overcome this bandwidth limitation is to break the long phase shifter into smaller segments and drive every segment with the same signal delayed by appropriate skew. This configuration can be interpreted as a Traveling Wave Electrode (TWE), as shown in Fig. 11. The fundamental idea underlying the TWE in contrast to lumped electrodes is the fact that the distributed capacitance does not limit the

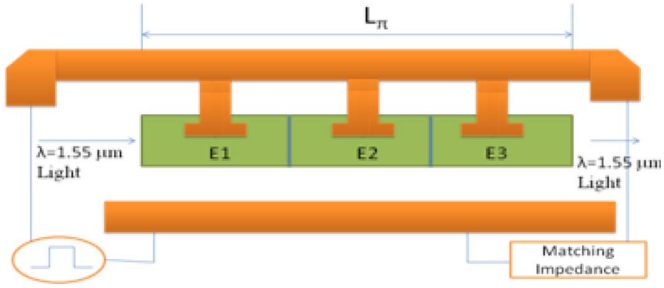

Fig. 11. Schematic of the emitter segmented modulator driven by TWE configuration. E1, E2, and E3 in the sketch denote the emitter segment 1, 2, and 3, respectively.

modulator speed [26]. Proper design will enable identical propagation speed of the optical and the modulating electrical signal, permitting the phase modulation to accumulate monotonically irrespective of frequency.

4.3. Optical Property Analysis

4.3.1. Refractive Index Profiles and Modal Characteristics

The total charge stored in the device in its spatial distribution under various V_{be} biases is extracted and imported to BPM for optical property analysis. The mode computation is done using the correlation method in the BPM simulation package as it has advantages for problems such as leaky, lossy, or radiating modes [18]. The wavelength is chosen as 1.55 μm. Electron and hole carrier distribution across the *XY* plane of the device is used to create the refractive index map. It is observed that the lateral confinement of the launched beam is achieved due to the silicon dioxide shallow trenches and deep trenches. However, vertical confinement is not achieved for the 1-μm deep subcollector because of the very small index difference between the base-collector region and the subcollector. Hence, the effect of reducing the thickness of subcollector on the electrical and optical properties of the SiGe HBT is investigated. Interestingly, reduction of subcollector thickness to 0.4 μm results in high vertical confinement of the optical modes. For a subcollector depth of 0.4 μm, the generated refractive index profiles for the SiGe base and the collector at a depth of 0.6 μm at V_{be} of 0 V and V_{be} of 1.1 V are generated. Using these refractive index profiles for subcollector depths of 1 μm and 0.4 μm, the mode profiles were computed.

A Gaussian beam of 1.3 μm $\times$ 1 μm is launched between the SiGe base and the subcollector along the length of the emitter. For a subcollector depth of 0.4 μm and a launch field of 1.3 μm $\times$ 1 μm, the single mode operation is verified.

4.3.2. Transmission Characteristics of L_π, Attenuation, and Extinction Ratio

The effective indices of the HBT waveguide are computed at different biasing conditions. Since Transverse Magnetic (TM) mode resulted in better interaction with free carrier plasma and, thus, smaller L_π, the following discussion is based on TM mode. The turn on switch is controlled by the V_{be} bias, varying between 0 V and 1.0 V or 1.1 V. In this paper, we analyze in detail how the subcollector thickness will affect the mode confinement L_π and attenuation loss. Because the variation of carrier concentration takes place near the base and the base-collector junction, it is favorable to push the optical mode closer to the base in order to obtain the maximum index modulation over the optical field. The mode profiles for the HBT with subcollector thicknesses (W_{sub}) of 1 μm and 0.4 μm under bias of 0 V and 1.1 V are shown in Fig. 12. Single-mode operation is verified by BPM mode solver for all conditions. For the case that the subcollector thickness is 1 μm, the emitter upper contour, the shallow trench, and the SiO_2 at the bottom of the device form a ridge-like waveguide structure. As the subcollector thickness is cut back, the shallow trench, having a total thickness of 0.6 μm measured from the top of the device, plays an increased role in confining

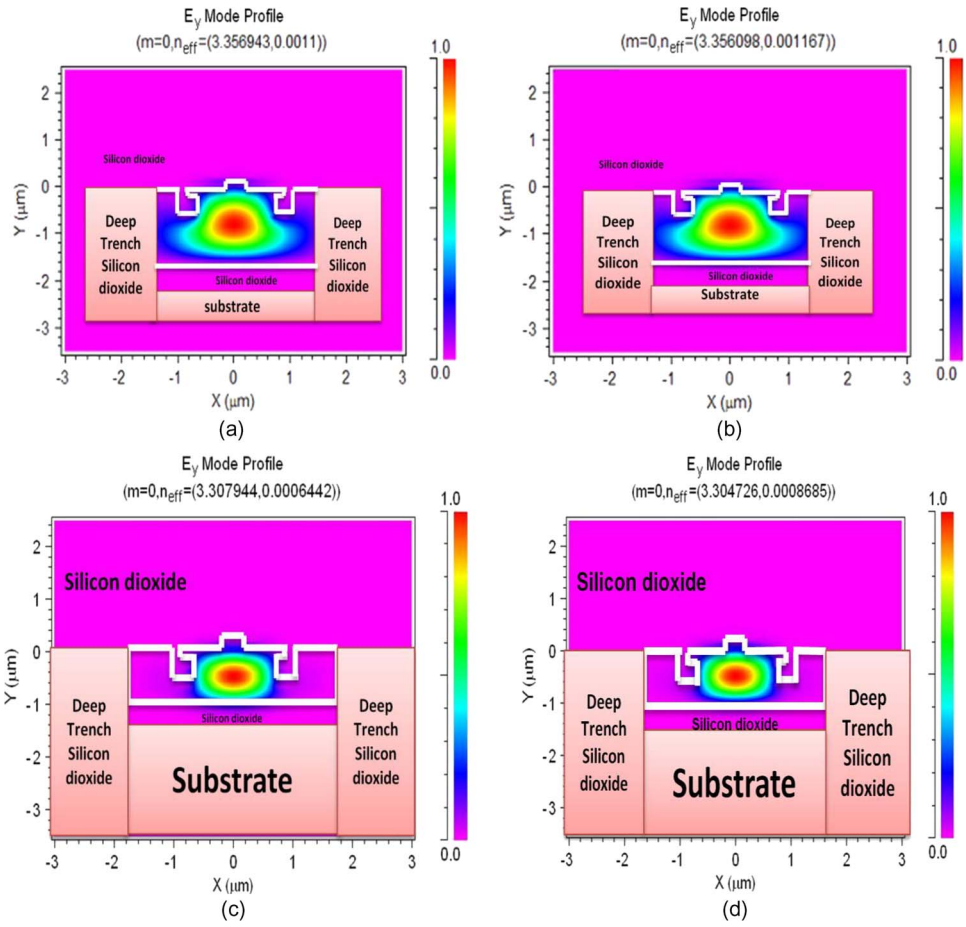

Fig. 12. Major electric field profiles at $\lambda = 1.55$ μm for quasi TM input (E_y), where W_{sub} = sub-collector depth. (a) $W_{sub} = 1$ μm and $V_{be} = 0$ V, (b) $W_{sub} = 1$ μm and $V_{be} = 1.1$ V, (c) $W_{sub} = 0.4$ μm and $V_{be} = 0$ V, and (d) $W_{sub} = 0.4$ μm and $V_{be} = 1.1$ V.

TABLE 1

Effect of sub-collector thicknesses on rise time, fall time, L_π, and propagation loss at $V_{be} = 1.1$ V

V_{be} (V)	T_r / T_f (ps)	W_{sub} (μm)	L_π (μm)	Propagation Loss (dB)
0-1.1V	4.8 / 3.2	1.0	917 (TM)	37.6
0-1.1V	5.1 / 3.6	0.4	240.8 (TM)	7. 36
0-1.1V	6.3 / 8.4	0.3	193.5 (TM)	6.082
0-1.1V	7.4 / 11.2	0.2	158.03 (TM)	5.33
0-1.1V	9.6 / 14.5	0.1	128.03 (TM)	5.12

the optical mode. For the case in which the subcollector thickness is cut back to 0.4 μm, the optical mode has a profile similar to that of a rectangular waveguide.

Table 1 above summarizes the rise time and fall time L_π and optical loss for various subcollector thicknesses. The rise and fall times increase as the subcollector thickness (W_{sub}) is cut back. This is because of the increase in the resistance of the subcollector to collector contact path. The decrease of L_π, as shown in Table 1, is anticipated as a result of enhanced optical wave and free carrier plasma interaction for thinner subcollector thickness. Within the collector region where the majority of the optical field is situated, the subcollector has the highest doping compared with the

TABLE 2
Summary of rise time, fall time, L_π, and Energy consumption per bit for different V_{be} bias voltages

V_{be} (V)	Rise time (ps)	Fall time (ps)	L_π (um)	Energy Consumption (fJ/bit)
0-1.1 V	5.1	3.6	240.8 TM	3600
0-1.0 V	4.6	1.54	1025 TM	1800

SIC region and the background doping in the collector. For a conventional HBT device, a high subcollector doping is used to reduce the resistance to the electrical contact. For an HBT on SOI or growth substrate removed, the electrical contact to the subcollector is optional. In the proposed HBT EO modulator design, we thinned down the subcollector thickness until it was totally removed. This leads to the sharp decrease in the loss due to attenuation from 0.041 dB/μm for a W_{sub} of 1 μm to 0.031 dB/μm for a W_{sub} of 0.4 μm. This can be easily explained from (2). Additional thinning of the subcollector region from W_{sub} of 0.4 μm only slightly impacts the waveguide loss. Through our study, we conclude that the doping concentration in the region occupied by the optical wave should be kept at or below $\sim 10^{18}$ cm^{-3} in order to maintain moderate propagation loss due to free carrier plasma scattering.

Clearly, there is a tradeoff between the rise/fall times and the mode confinement and, thus, L_π and loss figure. We chose W_{sub} of 0.4 μm as the optimal condition in this work. At V_{be} of 0 V, the effective index is computed as $3.307944 + j6.442 \times 10^{-4}$, and at V_{be} of 1.1 V, the effective index is computed as $3.304726 + j8.685 \times 10^{-4}$. For an MZI configuration, the L_π is computed to be 240.8 μm. The total optical beam propagation loss of the proposed HBT EO modulator is 7.36 dB. The corresponding voltage-length production, or the figure of merit (FoM), is 0.0264 V-cm for TM.

To evaluate how efficiently the light signal's intensity is modulated, extinction ratio can be examined as an indicator. It is defined as the ratio of the output intensity variations that represent logic level "1" (I_H) and "0" (I_L). The expression for extinction ratio in decibels can be written as $10 \times \log(I_H/I_L)$. In our proposed MZI structure, one arm is kept unbiased as a reference, while the other one is switched to produce the intensity difference. Considering the significant loss in the HBT EO modulator, both arms are equipped with the same HBT structure. In this way, the output intensity from each arm is comparable, and the extinction ratio is greatly improved. However, it is worth noting that despite the high extinction ratio value, a photodetector with high sensitivity is necessary because the absolute level of intensity is low as a result of the high loss. Denote the intensity at the output of the reference arm as I_1, and that on the modulation arm as I_2 and I_2' when the modulator is OFF and ON, respectively. Considering that the phase difference varies from 0 to ϕ when the output intensity changes from high to low, I_H and I_L is obtained as $I_H = I_1 + I_2 = 2I_1$, and $I_L = I_1 - I_2'$. The extinction ratio for the MZI structure is thus $10 \times \log[2I_1/(I_1 - I_2')]$. Based on the mode computation results reported above, the extinction ratio is calculated to be 7.5 dB when the EO modulator switches between 0 V and 1.1 V.

The proposed HBT has an electrical turn on voltage of V_{be} equal to $\sim$0.77 V. In this research, we also searched for the optimal operation voltage of the proposed device. The results are summarized in Table 2. For a V_{be} swing of 0 to 1.1 V and 0 to 1.0 V, the rise/fall times (1%–90%) of the carrier densities are 5.1 ps/3.6 ps and 4.6 ps/1.54 ps, while the L_π is 240.8 μm and 1025 μm, respectively. A more than four times difference in L_π is exhibited. The electron carrier density in the intrinsic base is 5×10^{19} cm^{-3} and 1×10^{20} cm^{-3} for the V_{be} swing of 0 to 1.0 V and 0 to 1.1 V, respectively. For this amount of difference in carrier concentration in the base, the large change in L_π seems unrealistic. However, looking at the optical modes [see Fig. 12(b) and (d)], it can be observed that the overlap between the electric field of fundamental mode and the charge carriers in the base is finite. To investigate this, a set of simulation experiments was conducted. In the first experiment, the base refractive index profile is varied for V_{be} of 0 V and V_{be} of 1.1 V, while that of the emitter and collector is kept unchanged. In the second experiment, the collector refractive index profile is varied for V_{be} of 0 V and V_{be} of 1.1 V, while the emitter and base are kept unchanged. It is observed that

the first experiment produced an L_π of 940 μm, while the second predicted an L_π of 360 μm. This shows that the free carrier plasma in the collector is primarily responsible for the change in effective index rather than the free carrier plasma in the base.

4.4. Dynamic Power Consumption

The dynamic power of the device of 240.8 μm lengths is evaluated by (4) [19]:

$$P_d = 0.5 \times f_s \times \int_0^{T_s} (i_c(t) V_{\text{ce}}(t) + i_b(t) V_{\text{be}}(t))\, dt \tag{4}$$

where, f_s is the switching frequency, T_s is the pulse duration, i_c is the collector current, and i_b is the base current. The factor 0.5 in (4) accounts for the fact that the "ON" state appears with 50% possibility in a long random Non-Return-to-Zero (NRZ) pulse train. The minimum pulse width, or the maximum data rate, is limited by the response time. According to our transient analysis, the smallest T_s is 12.5 ps, and the inverse of T_s gives a maximum Baud rate of 80 Gbit/s. Based on the above assumption, the dynamic energy consumption is 3.6 pJ/bit at V_{be} of 1.1 V, which is lower than 5 pJ/bit [5] but higher than that of 400 fJ/bit [20]. To enhance this basic HBT modulation, it will be necessary to devise a low Q resonator that is compatible with the HBT electrical structure and will still permit a small amount of reuse of the plasma. Based upon prior work, an assumed Q of only 10–30 could considerably shorten the device and lower its power consumption accordingly [23]. A patent application has also recognized that plasma dispersion effect can be used to modulate light in a graded base SiGe HBT enhanced by using a low Q resonator structure for plasma reuse [21].

5. Conclusion

This paper reports the detailed device structure design as well as the electrical and optical property analysis of an 80-Gbit/s SiGe EO modulator. Positive ramp voltages of 1.0 V and 1.1 V for 1-ps ramp time are applied at the base and free carrier dispersion effect is utilized to achieve an EO modulation. An L_π of 240.8 μm is modeled with rise and fall times of 5.1 and 3.6 ps, respectively, for a 0.4-μm subcollector and an L_π of 193.5 μm with rise and fall times of 6.3 and 8.4 ps, respectively, for 0.3-μm subcollector depth at V_{be} of 1.1 V bias. Additionally, for a V_{be} bias of 1.0 V and a subcollector depth of 0.4 μm, an L_π of 1025 μm is simulated with rise and fall times of 4.56 and 1.54 ps, respectively. With these excellent results, we report the modeling of an 80-Gbit/s SiGe HBT EO modulator attractive for high-speed silicon photonic integrated circuits. Further improvements in L_π can be made by slow light interaction with the carrier plasma without degrading the operation speed. In addition, the compatibility of the terminal characteristics of the HBT with the IBM 8HP technology suggests the possibility of fast deployment of the proposed HBT EO modulator.

Acknowledgment

The authors wish to express their deepest thanks to Dr. H. D. Dardy for providing inspiration for this research and his enthusiastic support during his lifetime.

References

[1] J. A. Kash, "Leveraging optical interconnects in future supercomputers and servers," in *Proc. 16th IEEE Symp. HOTI*, Aug. 26–28, 2008, pp. 190–194.
[2] R. S. Jacobsen, K. N. Andersen, P. I. Borel, J. Fage-Pedersen, L. H. Frandsen, O. Hansen, M. Kristensen, A. V. Lavrinenko, G. Moulin, H. Ou, C. Peucheret, B. Zsigri, and A. Bjarklev, "Strained silicon as a new electro-optic material," *Nature*, vol. 441, no. 7090, pp. 199–202, May 2006.
[3] Y. H. Kuo, Y. K. Lee, Y. Ge, S. Ren, J. E. Roth, T. I. Kamins, D. A. Miller, and J. S. Harris, "Strong quantum-confined Stark effect in germanium quantum well structures on silicon," *Nature*, vol. 437, no. 7063, pp. 1334–1336, Oct. 2005.
[4] R. A. Soref and B. R. Bennett, "Electrooptical effects in silicon," *IEEE J. Quantum Electron.*, vol. QE-23, no. 1, pp. 123–129, Jan. 1987.

[5] A. Cutolo, M. Iodice, P. Spirito, and L. Zeni, "Silicon electro-optic modulator based on a three terminal device integrated in a low-loss single-mode SOI waveguide," *J. Lightw. Technol.*, vol. 15, no. 3, pp. 505–518, Mar. 1997.
[6] W. M. Green, M. J. Rooks, L. Sekaric, and Y. A. Vlasov, "Ultra-compact, low RF power, 10 Gb/s silicon Mach–Zehnder modulator," *Opt. Express*, vol. 15, no. 25, pp. 17 106–17 113, Dec. 2007.
[7] A. Liu, L. Liao, D. Rubin, H. Nguyen, B. Ciftcioglu, Y. Chetrit, N. Izhaky, and M. Paniccia, "High-speed optical modulation based on carrier depletion in a silicon waveguide," *Opt. Express*, vol. 15, no. 2, pp. 660–668, Jan. 2007.
[8] F. Gardes, G. Reed, N. Emerson, and C. Png, "A sub-micron depletion-type photonic modulator in silicon on insulator," *Opt. Express*, vol. 13, no. 22, pp. 8845–8854, Oct. 31, 2005.
[9] Q. Xu, B. Schmidt, S. Pradhan, and M. Lipson, "Micrometre-scale silicon electro-optic modulator," *Nature*, vol. 435, no. 7040, pp. 325–327, May 2005.
[10] R. D. Lareau, L. Friedman, and R. A. Soref, "Waveguided electro-optical intensity modulation in a $Si/Ge_xSi_{1-x}/Si$ heterojunction bipolar transistor," *Electron. Lett.*, vol. 26, no. 20, pp. 1653–1655, Sep. 27, 1990.
[11] B. Li, G. Li, E. Liu, Z. Jiang, C. Pei, and X. Wang, "1.55 μm reflection type optical waveguide switch based on SiGe/Si plasma dispersion effect," *Appl. Phys. Lett.*, vol. 75, no. 1, pp. 1–3, Jul. 1999.
[12] B. Li, Z. Jiang, X. Zhang, X. Wang, J. Wan, G. Li, and E. Liu, "SiGe/Si Mach–Zehnder interferometer modulator based on the plasma dispersion effect," *Appl. Phys. Lett.*, vol. 74, no. 15, pp. 2108–2109, Apr. 1999.
[13] D. Marries, E. Cassan, L. Vivien, D. Pascal, A. Koster, and S. Laval, "Design of a modulation-doped SiGe/Si optical modulator integrated in a submicrometer silicon-on-insulator waveguide," *Opt. Eng.*, vol. 4, no. 8, pp. 084001–084002, Aug. 2005.
[14] B. Jagannathan, M. Khater, F. Pagette, J.-S. Rieh, D. Angell, H. Chen, J. Florkey, F. Golan, D. R. Greenberg, R. Groves, S. Jeng, J. Johnson, E. Mengistu, K. Schonenberg, C. Schnabel, P. Smith, A. Stricker, D. Ahlgren, and G. Freeman, "Self-aligned SiGe NPN transistors with 285 GHz f_{MAX} and 207 GHz f_T in a manufacturable technology," *IEEE Electron Device Lett.*, vol. 23, no. 5, pp. 258–260, May 2002.
[15] *Taurus Medici User Guide,* Synopsys, Mountain View, CA, Mar. 2007, ver. Z-2007.03.
[16] D. B. M. Klaassen, J. W. Slotboom, and H. C. de Graaff, "Unified apparent bandgap narrowing in n- and p-type silicon," *Solid State Electron.*, vol. 35, no. 2, pp. 125–129, Feb. 1992.
[17] M. Host, P. Brenner, and R. Lachner, "Investigation of advanced SiGe heterojunction bipolar transistors at high power densities," in *Proc. Meeting Bipolar/BiCMOS Circuits Technol.*, Sep. 13–14, 2004, pp. 100–103.
[18] *BeamProp 8.1 Manual,* Rsoft Design Group, Ossining, NY. [Online]. Available: http://www.rsoftdesign.com
[19] S. Deng, T. G. Neogi, J. Novak, J. McDonald, and R. Huang, "Design of short electro-optic modulator based on SiGe HBT structure," *Opt. Express*, vol. 18, no. 3, pp. 1994–2001, Jan. 2010.
[20] X. Zheng, J. Lexau, Y. Luo, H. Thacker, T. Pinguet, A. Mekis, G. Li, J. Shi, P. Amberg, N. Pinckney, K. Raj, R. Ho, J. E. Cunningham, and A. V. Krishnamoorthy, "Ultra-low-energy all-CMOS modulator integrated with driver," *Opt. Express*, vol. 18, no. 3, pp. 3059–3070, Jan. 2010.
[21] J. F. McDonald, H. D. Dardy, and J.-R. Guo, "Direct Light Modulation in Silicon With a Graded Base SiGe HBT Through its Carrier Plasma—Using 3D Wafer Stacking Techniques to Incorporate a Photonic Slow Wave Device into the Drude Effect Phase Shifter and Associated Photonic Waveguide," in *NRL disclosure #97873*, Mar. 2005, provisional patent application 61/310754. Filed March 5, 2010.
[22] [Online]. Available: http://www.mosis.com/ibm/
[23] Y. Jiang, W. Jiang, L. Gu, X. Chen, and R. T. Chen, "80-micron interaction length silicon photonic crystal waveguide modulator," *Appl. Phys. Lett.*, vol. 87, no. 22, p. 221 105, Nov. 2005.
[24] S. Deng, Z. Rena Huang, and J. McDonald, "Design of high efficiency multi-GHz SiGe HBT electro-optic modulator," *Opt. Express*, vol. 17, no. 16, pp. 13 425–13 428, Jul. 2009.
[25] Y. Tang, "Study on electro-absorption modulators and grating couplers for optical interconnects," Ph.D. dissertation, Roy. Inst. Technol., Stockholm, Sweden, 2010.
[26] H. Chen, "Development of an 80 Gbit/s InP-based Mach–Zehnder modulator," Ph.D. dissertation, Berlin Univ. Technol., Berlin, Germany, 2007.
[27] C. T. Shih, Z. W. Zeng, and S. Chao, "Design and analysis of metal-oxide-semiconductor-capacitor microring optical modulator with solid-phase-crystallization poly-silicon gate," *J. Lightw. Technol.*, vol. 27, no. 17, pp. 3861–3873, Sep. 1, 2009.
[28] Y. Ishikawa and K. Wada, "Near-infrared Ge photodiodes for Si photonics: Operation frequency and an approach for the future," *IEEE Photon. J.*, vol. 2, no. 3, pp. 306–320, Jun. 2010.
[29] J. D. Cressler, *Silicon Heterostructure Handbook: Materials, Fabrication, Devices, Circuits and Applications of SiGe and Si Strained-Layer Epitaxy*. New York: CRC, 2005, 1210 pp.
[30] S. Manipatruni, Q. Xu, B. Schmidt, J. Shakya, and M. Lipson, "High speed carrier injection 18 Gb/s silicon micro-ring electro-optic modulator," in *Proc. 20th Annu. Meeting IEEE LEOS*, Oct. 21–25, 2007, pp. 537–538.
[31] K. K. Lee, "Transmission and routing of optical signals in on-chip waveguides for silicon micro photonics," Ph.D. dissertation, Mass. Inst. Technol., Cambridge, MA, 2001.